

ORIGINAL ARTICLE

A step toward engineering thick tissues: Distributing microfibers within 3D printed frames

Joseph Molde | Joseph A. M. Steele | Alexandra K. Pastino | Anisha Mahat |
N. Sanjeeva Murthy | Joachim Kohn

New Jersey Center for Biomaterials,
Rutgers – The State University of New Jersey,
Piscataway, NJ

Correspondence

Joachim Kohn, New Jersey Center for
Biomaterials, Rutgers – The State University of
New Jersey, Piscataway, NJ 08854, USA.
Email: kohn@dls.rutgers.edu

Funding information

National Institute of Health, Grant/Award
Number: P41EB001046

Abstract

Microfiber mats for tissue engineering scaffolds support cell growth, but are limited by poor cell infiltration and nutrient transport. Three-dimensional printing, specifically fused deposition modeling (FDM), can rapidly produce customized constructs, but macroscopic porosity resulting from low resolution reduces cell seeding efficiency and prevents the formation of continuous cell networks. Here we describe the fabrication of hierarchical scaffolds that integrate a fibrous microenvironment with the open macropore structure of FDM. Biodegradable tyrosine-derived polycarbonate microfibers were airbrushed iteratively between layers of 3D printed support structure following optimization. Confocal imaging showed layers of airbrushed fiber mats supported human dermal fibroblast growth and extracellular matrix development throughout the scaffold. When implanted subcutaneously, hierarchical scaffolds facilitated greater cell infiltration and tissue formation than airbrushed fiber mats. Fibronectin matrix assembled in vitro throughout the hierarchical scaffold survived decellularization and provided a hybrid substrate for recellularization with mesenchymal stromal cells. These results demonstrate that by combining FDM and airbrushing techniques we can engineer customizable hierarchical scaffolds for thick tissues that support increased cell growth and infiltration.

KEYWORDS

3D Printing, Fused Deposition Modeling, Airbrushing, Solution Blow Spinning, Hierarchical Scaffold, Extracellular Matrix, Scaffold Fabrication

1 | INTRODUCTION

Biodegradable nanofiber and microfiber scaffolds are used extensively to support the attachment and proliferation of cells for tissue engineering applications (Agarwal, Wendorff, & Greiner, 2008; Agarwal, Wendorff Joachim, & Greiner, 2009; Moroni, Schotel, Hamann, de Wijn, & van Blitterswijk, 2008; Sill & von Recum, 2008). These structures provide high surface areas for cell attachment, often furnishing a temporary substrate upon which natural extracellular matrix (ECM) can be developed to achieve tissue regeneration. Electrospinning is a commonly employed method for fabricating nano- or microfiber

meshes for tissue engineering applications (Acun & Hasirci, 2014; Ahn et al., 2019; de Valence et al., 2012; Jeong et al., 2004; Kong et al., 2017; Lannutti, Reneker, Ma, Tomasko, & Farson, 2007; Park et al., 2009; Sheihet et al., 2008; Soletti et al., 2011; Wang, Ding, & Li, 2013; Wray & Orwin, 2009; Yang, Murugan, Wang, & Ramakrishna, 2005; Yoshimoto, Shin, Terai, & Vacanti, 2003; Zhu, Cui, Li, & Jin, 2008). Electrospinning involves using an electric field to draw continuous polymer fiber from a syringe to a substrate where a nonwoven mat is formed. Though electrospinning has seen extensive use, it possesses significant limitations as a manufacturing process. Fabricating electrospun mats of significant thickness takes hours to complete with

This is an open access article under the terms of the Creative Commons Attribution-NonCommercial-NoDerivs License, which permits use and distribution in any medium, provided the original work is properly cited, the use is non-commercial and no modifications or adaptations are made.

© 2019 The Authors. *Journal of Biomedical Materials Research Part A* published by Wiley Periodicals, Inc.

deposition rates limited to 0.025 ml/min (Beachley & Wen, 2009). Furthermore, the electrical potential driving force required to draw fibers from the syringe limits the variety of substrates that can be targeted for fiber deposition. Airbrushing is an alternative method that overcomes some of these problems in fabricating fibrous mats. Although airbrushing is not as widely used as electrospinning, it offers significant benefits over the latter, especially in the context of transplantable tissue engineering technologies and integration with existing manufacturing methods like 3D printing (Daristotle, Behrens, Sandler, & Kofinas, 2016). Airbrushed fiber mats are fabricated using a commercial airbrush that costs a fraction of the price of an electrospinning setup. This process mimics industrial-style fiber mat fabrication and is much faster, taking only seconds to minutes to build a mat of significant thickness with deposition rates of 0.1 ml/min or more (Behrens et al., 2016; Medeiros, Glenn, Klamczynski, Orts, & Mattoso, 2009; Oliveira et al., 2011). The significantly lower fabrication time reduces associated costs and lead time on device production. Fibers produced by this method can be deposited on any substrate, including *in vivo*, providing much greater flexibility in application over electrospinning (Behrens et al., 2014).

However, a challenge faced by both electrospun and airbrushed fiber mats is the ability to promote cell infiltration and nutrient transport in mats of a significant thickness (Rnjak-Kovacina & Weiss, 2011). Impaction of the fibers upon the deposition surface limits the overall porosity by compressing the structure into a nearly two-dimensional sheet. This results in limited three-dimensional volume and smaller pore sizes while also being weak mechanically and difficult to handle. These are areas where the incorporation of 3D printing techniques is beneficial.

The flexibility and speed of airbrushing allow for nearly seamless integration with 3D printing technologies (Behrens et al., 2014; Chen, Townsend, Sell, & Martin, 2017). 3D printing has emerged as a means to rapidly create centimeter-scaled tissue scaffolds with customizable shape and structure (Chia, 2015; Huttmacher Dietmar et al., 2001). Fused deposition modeling (FDM) is attractive for its relative ease of use, structure customization, rapid prototyping ability, low cost, and wide polymer compatibility, including biocompatible materials like polylactic acid (PLA), polycaprolactone (PCL), and polylactic-co-glycolic acid (PLGA). However, the ratio of strut size to pore size in these scaffolds is inefficient for cell culturing which limits their promise in tissue regeneration applications. The minimum filament diameter producible from FDM machines is on the order of 200 μm while spatial precision in the *x-y* plane is near 10 μm . The layer thickness, or *z* resolution, is limited by the nozzle thickness and is on the order of 60 μm (Kuznetsov, Solonin, Urzhumtsev, Schilling, & Tavittov, 2018). The optimal pore size range for tissue engineering is considered 50–300 μm (Karageorgiou & Kaplan, 2005; Oh, Park, Kim, & Lee, 2007). These pore sizes are theoretically achievable with FDM, however, the porosity in such a scaffold would be below 60% as constrained by the diameter of the printed struts. Large, open macroporous structure of 3D printed scaffolds provides minimal surface area for cell attachment and growth. Airbrushing can be used to provide additional surface area within the 3D printed scaffold

macropores for cell growth and development while minimally affecting the overall porosity of the devices. The framework of the 3D printed struts separates the airbrushed layers while maintaining the porosity of the fiber mat. Furthermore, cells rely on signaling cues and attachments points from the underlying matrix which are absent in scaffolds printed by FDM but could be provided in airbrushed fiber mats. Overall, the benefits of and challenges faced by FDM make it a perfect pairing for airbrushed fiber mat integration (Chen et al., 2019; De Mori, Peña Fernández, Blunn, Tozzi, & Roldo, 2018; Mellor et al., 2017; Moroni et al., 2008; Rampichová et al., 2018).

Based on these considerations, we have developed a method of creating hierarchical scaffolds combining airbrushed microfiber mats periodically interspersed within a FDM 3D printed support as a way to open up the fiber mat structure to allow for improved cell penetration while maintaining the rapid manufacturing and customization and improving the cell interactivity of 3D printed scaffolds. The airbrushed mat is formed out of a biodegradable tyrosine polycarbonate that has been used for bone regeneration in the past and degrades on the time frame of months allowing for the natural ECM to take over (Jinku et al., 2015; Kim et al., 2015; Zhang et al., 2016). Culturing human dermal fibroblasts upon the scaffold prior to decellularization allowed for the functionalization of the hierarchical scaffold with cell-derived ECM to create a hybrid natural and synthetic structure. These hierarchical scaffolds show cell penetration, extensive fibronectin deposition from cells cultured on the scaffolds, durability during processing, and improved tissue integration *in vivo*. Using this approach, we have harnessed the benefits of both airbrushing and 3D printing methods to create a versatile scaffold for engineering thick tissues.

2 | MATERIALS AND METHODS

2.1 | Airbrushed fiber mats

Solutions for airbrushing were prepared by dissolving E1001 (1k), a tyrosine-derived polycarbonate, in 3 ml of tetrahydrofuran (THF) to get to a range of final concentrations from 5% to 10% w/v. In the notation $\text{Exyyy}(\text{nk})$, the *xx* and *yy* are the percent mole fractions of desaminotyrosol-tyrosine (DT) and poly(ethylene glycol) (PEG) with the molecular weight, *n*, in kDa; the remainder is desaminotyrosol-tyrosine ethyl ester (DTE; Magno et al., 2010; Yu & Kohn, 1999). Solutions were mixed on a rotating shaker plate until all polymer dissolved. The polymer airbrushing solution was loaded into the holding chamber of a commercial painting airbrush (Master Airbrush, G222-Set, 0.5 mm nozzle, dual-action, gravity fed). The airbrush was connected to 25 psi dry nitrogen source and the tip was stored in THF when not in use to prevent clogging. With the dual-action airbrush, depressing the trigger began airflow over the airbrush tip, while pulling back on the trigger initiated solution flow and fiber deposition. During optimization, airbrushing distance was varied from 10 to 20 cm, time from 3 to 9 s, and nitrogen pressure from 15 to 25 psi. The tensile modulus of the airbrushed and randomly oriented electrospun fiber mats was measured using a dynamic mechanical analyzer (Sintech 5/D, MTS Systems Corporation) set up for tensile testing. The molecular weight

of E1001 (1k) before and after airbrushing was measured by gel permeation chromatography (GPC, Waters 515 HPLC Pump, 717 Autosampler, 2414 Detector, Agilent PLgel 5 μm 10 \AA , 2 columns) relative to a polystyrene standard ($n = 1$).

2.2 | Scaffold fabrication

Orthogonal log-stack scaffolds for 3D printing were designed using CAD software (Sketchup, Trimble Inc.) with 1.5 mm spacing between each strut, with strut dimensions of $0.5 \times 0.25 \times 27$ mm. Each scaffold was 10 layers tall with a 90° rotation between each layer to make a box pattern. Open source software (ReplicatorG) was used to convert the STL file to a G-code for printing. A pause command was added after every other layer to allow for airbrushing of the scaffold in situ. Scaffolds were printed using a commercial fused deposition modeling style 3D printer (Makerbot Replicator 2, Makerbot) and commercial 1.75 mm PLA filament (Makerbot PLA Filament, Makerbot) at 215°C or PCL at 110°C (Makerbot Flexible Filament, Makerbot). At each pause, a layer of airbrushed fibers was deposited on the scaffold from a distance of 20 cm using 25 psi nitrogen for 3 s. Completed scaffolds were cut into quarters with final dimensions of $12.5 \text{ mm} \times 12.5 \text{ mm} \times 2.5 \text{ mm}$. Scaffolds for in vitro and in vivo analysis were sterilized by exposure to ethylene oxide (Anaspec 70, Anprolene) for 12 hr.

2.3 | Scanning electron microscopy

Sections of the scaffold were attached to aluminum sample pegs using double-sided conductive adhesive tape. Sample pegs were placed on a charge reducing sample holder, which was loaded into the SEM (Phenom ProX, Phenom World, 10 kV). Images were acquired at three different locations at low (255 \times) and high (1,000 \times) magnifications.

2.4 | Micro-computed tomography

Scaffold with and without airbrushed fiber mats were imaged on a Skyskan1172 at the Rutgers University Molecular Imaging Center ($n = 1$). Images were acquired at 34 kV, 210 μA , 0.3° step size, and voxel dimension of 1.92 μm . Images were reconstructed with CTAn (Bruker) and 3D rendered with FIJI.

2.5 | Fiber mat characterization

Coverage of the airbrushed fiber mats was determined from SEM images using ImageJ thresholding to differentiate fiber from pore. The covered area was calculated from the thresholded image. Fiber diameters were measured manually using ImageJ from SEM images. The number of fiber defects was counted using the ImageJ cell counter plugin. Micro-CT images were processed in FIJI to determine the porosity of the hierarchical scaffolds. Porosity was determined from thresholded image stacks representing one unit cell of hierarchical scaffold or pore.

2.6 | Scaffold mechanical analysis

Mechanical properties of hierarchical and empty 3D printed scaffolds were evaluated using a dynamic mechanical analyzer (Sintech 5/D, MTS Systems Corporation) by compression testing. Each 10-layer scaffold was cut to $5 \text{ mm} \times 5 \text{ mm}$ in size prior to testing ($n = 3$). Scaffolds were compressed to 50% strain or to the 1000 N load cell limit, whichever was reached first, at a rate of 5 mm/min. Young's modulus was calculated from the linear portion of the stress-strain curve.

2.7 | AFM analysis

Mechanical properties of airbrushed fibers were assessed using AFM (Nanosurf AG, Switzerland) and ACLA-50 contact-mode cantilever with a stiffness of 48 N/m (AppNano). The scaffold used for these tests ($n = 1$) was 3D printed struts with sparse, airbrushed E1001 (1k) fibers across 2 mm gaps, cut into a small piece, fitted into a small petri dish using silly putty, and then mounted on a microscope under the AFM scan head. The force spectroscopy was performed using a distance of 50 μm so the full behavior of the cantilever acting on the fiber can be captured. The speed of the cantilever was 1 $\mu\text{m}/\text{s}$ and the setpoint was 100–400 nN. The maximum calibrated deflection was 730 nm. Several data points were taken on multiple fibers across the 2 mm gap.

2.8 | Cell culture and decellularization

Human Dermal Fibroblasts (HDF; ATCC) under passage 10 were expanded in high glucose Dulbecco's Modified Eagle's Media (DMEM; Gibco) supplemented with 10% fetal bovine serum (Atlanta Biologicals) and 0.1% gentamycin (Sigma). Sterilized hierarchical scaffolds were placed in individual wells of a nontissue culture polystyrene 24-well plate and seeded at a density of 1×10^4 cells/ mm^2 in 0.5 ml medium. Scaffolds were placed on a rocker for 1 hr at 37°C , after which 1.5 ml of media was added and the plate was incubated without shaking for 7 days. For decellularization, a published protocol (Mao and Schwarzbauer, 2005) was used except that the second incubation in lysis buffer was for 90 min, 37°C . Matrices were stored in PBS at 4°C for at least 48 hr before reseeding with cells.

Human mesenchymal stromal cells (MSCs, Texas A&M) under passage 5 were expanded in Minimal Essential Medium Eagle-Alpha Modification (α -MEM; Gibco), supplemented with 10% fetal bovine serum (Atlanta Biologicals) and 0.1% gentamycin (Sigma). Human mesenchymal stromal cells (MSCs, Texas A&M) were plated in basal medium on scaffolds with decellularized ECM at 2×10^4 cells/well in a 24-well nontissue culture-treated plate. Cells were rocked gently on an orbital shaker for 1 hr before static incubation for a total of 24 hr.

2.9 | Immunostaining and imaging

After incubation, scaffolds were fixed in 4% paraformaldehyde solution (Affymatrix/USB) with gentle rocking for 15 min at room temperature and washed three times with PBS. Scaffolds were blocked with

5% goat serum (Sigma) for 1 hr at room temperature followed by TrueBlack autofluorescence blocking (Biotium) for 60 s according to the supplied protocol. After three PBS washes, scaffolds were incubated with a polyclonal fibronectin antibody (Invitrogen, PA5-29578; 1:100 dilution) in 2% ovalbumin (Sigma) for 1 hr at room temperature with slight shaking on an orbital shaker. The scaffolds were again washed twice with PBS. A secondary staining solution containing Hoechst (AnaSpec; 1:500) for nuclei staining, actin stain with phalloidin 594 (Invitrogen) at 1:20 dilution or rhodamine-phalloidin (Thermo Fisher) at 1:50 dilution where indicated, and Alexa Fluor goat anti-rabbit (488 or 633 where indicated; Invitrogen; 1:500) in 2% ovalbumin was added and incubated in the dark at room temperature with slight shaking for 1 hr. After staining, the scaffolds were washed twice with PBS and stored at 4°C until imaging.

Scaffolds were imaged on a multiphoton TCS SP2 confocal microscope. Maximum intensity projections and z-stacks through the depth of the scaffold were collected. Scaffolds were bisected to image the cross-sectional distribution of cells and fibronectin with maximum intensity projections.

2.10 | In vivo analysis

An in vivo subcutaneous analysis was performed to evaluate cellular penetration at 14 days into the hierarchical scaffolds and airbrushed fiber mat controls. Procedures were reviewed and approved by the Rutgers University Institutional Animal Care and Use Committee (IACUC). The airbrushed fiber mat controls were composed of E1001 (1k) airbrushed fibers deposited as a mat 1 mm in thickness. The hierarchical scaffolds were composed of E1001 (1k) airbrushed fibers and poly(caprolactone) 3D printed struts. Scaffolds were terminally sterilized by exposure to ethylene oxide for 12 hr (Anaspec 70). Male Sprague–Dawley rats (12 weeks old, 350 g, Charles River) were anesthetized by isoflurane (2% v/v) and treated with buprenorphine (general analgesic, 0.075 mg/kg s.c.), bupivacaine (local anesthetic, 2 mg/kg s.c.), and Baytril (antibiotic, 5 mg/kg s.c.). The dorsal region was shaved and sterilized with three iterative betadine and isopropanol washes. Up to four 10 mm cutaneous incisions were made, 10 mm from the midline, and pockets were bluntly dissected to 10 × 10 mm². Sterile implants ($n = 4$) or controls ($n = 2$) were placed within the pockets, closed by a 9-mm wound closure clip. Animals were euthanized by exposure to CO₂, 14 days after implantation. Scaffolds and the overlying skin were collected and fixed in 10% formalin for 48 hr at room temperature.

2.11 | Histology

Fixed samples were embedded in paraffin and sectioned (Rutgers University Office of Research Commercialization Pathology Services). Paraffin sections (4 μm) were dewaxed, hydrated, stained by hematoxylin and eosin (H&E), and dehydrated following standard protocols. H&E sections were digitized on a Zeiss transmitted light microscope.

2.12 | Statistical analysis

Significance was verified using the Student's *t*-test and expressed as the mean ± standard deviation for a minimum of three measurements. Statistical significance was shown by * for $p < .05$.

3 | RESULTS

3.1 | Optimization of airbrushed mats

Airbrushed fiber mat morphology was optimized by tuning air pressure, polymer concentration, spray duration, and collector plate distance. Pressures below 20 psi did not produce adequate shearing forces at the tip of the airbrush nozzle to form fibers, resulting in an increased number of beading defects. Increasing the pressure above 30 psi resulted in fiber whipping behavior and excessive force and damage to the deposited fiber mat. Therefore, subsequent experiments used a feed pressure of 25 psi. The concentration of E1001 (1k) polymer solutions in THF tested ranged from 5 to 10 w/v%. Fiber diameter increased with solution concentration, ranging from 1.9 ± 0.5 μm at 5 w/v% to 3.4 ± 1.2 μm at 10 w/v% (Figure 1c). Defects, defined as polymer beading along the length of the fibers, were observed to varying degrees at all concentrations. The number of fiber defects increased with solution concentration, ranging from 0.6 ± 0.1 defects per fiber to 1.1 ± 0.1 defects per fiber, for 5 w/v% and 10 w/v%, respectively (Figure 1d). Above 10 w/v%, the solution was too viscous pass through the airbrush nozzle without clogging. From these results, we determined the optimal concentration for E1001 (1k) fiber formation from airbrushing was 6% w/v to minimize fiber defects and reduce fiber diameter. The molecular weight of the E1001 (1k) was at 206 kDa before and after airbrushing (Figure S1).

Once polymer concentration was set, the airbrushing distance (10–20 cm) and duration (3–9 s) were investigated to determine optimal fiber mat distribution. SEM images were thresholded in ImageJ to calculate the fiber coverage area and plotted against time and distance (Figure 1e). At a distance of 10 cm, the density of polymer fibers was highest at all time points investigated. Increasing the airbrushing duration from 3 to 9 s at 10 cm decreased fiber mat porosity from 40% to 13%. However, 10 cm of distance did not allow for sufficient solvent evaporation, resulting in a wet mat with film formation at 6 and 9 s. Increasing the distance to 20 cm was ideal for consistent fiber formation, with coverage of 77, 62, and 48% for 3, 6, and 9 s, respectively. Distances beyond 20 cm resulted in fewer fibers landing on the substrate and reduced control over the deposition location and fiber density. Therefore, the optimal airbrushing conditions for 33 kDa E1001 (1k) of 6 w/v%, 25 psi, 20 cm displacement and 3 s duration were used in scaffold fabrication for subsequent experiments.

3.2 | Hierarchical scaffolds

In order to increase the porosity of the airbrushed fiber mat, a hierarchical scaffold approach was developed by iteratively airbrushing E1001 (1k) and 3D printing PLA or PCL struts. The 3D printed

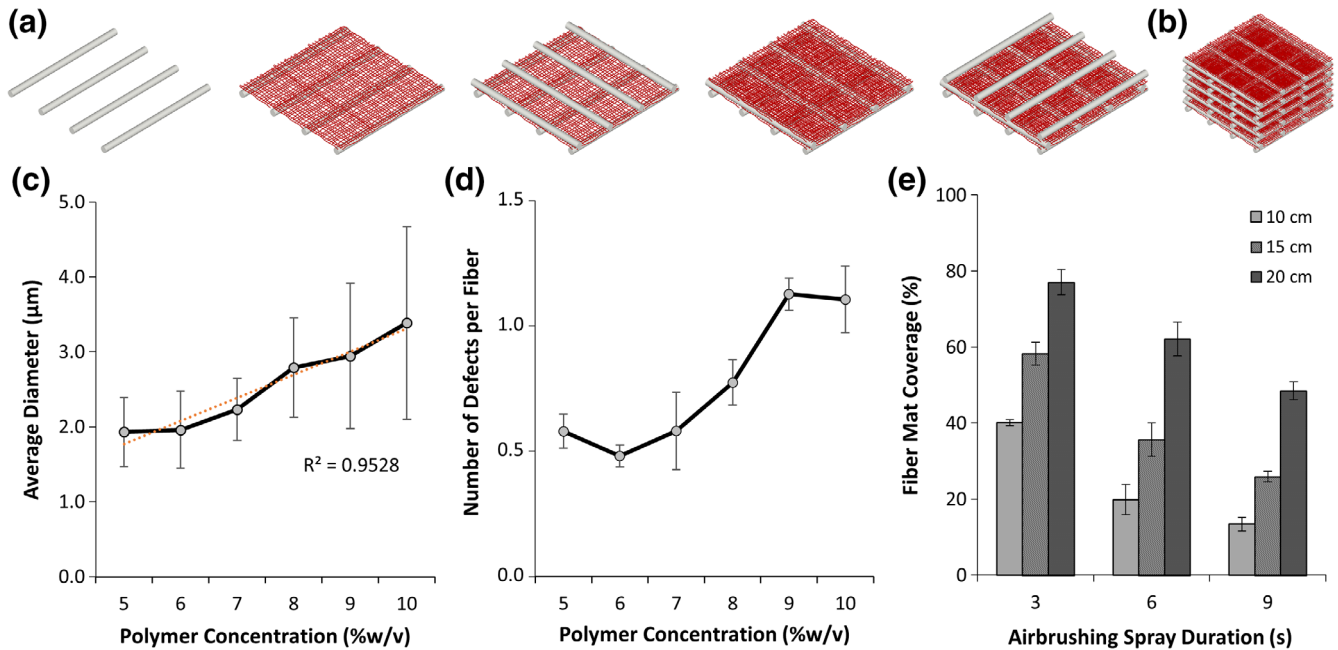


FIGURE 1 Hierarchical scaffolds were produced from the iterative integration of fused deposition modeling (FDM) and airbrushing. (a) Stepwise schematic of scaffold production where airbrushed fibers layers are deposited between orthogonal FDM struts. (b) Schematic of complete hierarchical scaffold. (c) Average fiber diameter as a function of polymer concentration. (d) Average number of defects per fiber as a function of polymer concentration. (e) Fiber coverage area as a function of airbrush spray duration and distance ($n = 3$, \pm SD)

portions of the scaffolds were simple orthogonal log stack structures with 1.5 mm spacing between parallel struts. E1001 (1k) has a T_g of 90°C so printing with PCL at 110°C facilitated fusion between the struts and E1001 (1k) without damaging the fiber mats. In contrast, printing with PLA at 215°C caused the E1001 (1k) fiber mats to melt and fall away from the struts. Full hierarchical scaffold porosity was determined by micro-CT analysis of the optimized structures (Figure 2d–f). The 3D printed struts comprised 27% of the scaffold volume while the E1001 (1k) airbrushed fibers made up an additional 3% in sheet-like layers between each layer of struts. This gives the hierarchical scaffolds an overall porosity of 70%.

The 3D printed structure provided support and protection for the more delicate airbrushed fiber network during handling, sterilization, and implantation. The Young's modulus of a combined E1001 (1k)-PLA scaffold under compression (25 ± 4 MPa) was not statistically different than the PLA struts alone (28 ± 1 MPa), suggesting that the mechanical strength is determined by the 3D struts (Figure 3b). The absence of delamination during testing and handling indicates that the strut and fiber mat layers are effectively fused during printing.

The tensile properties of the airbrushed E1001 (1k) fibers were assessed both in bulk by mechanical tests and microscopically by AFM. AFM is a unique means of measuring localized and individual fiber mechanical properties on a cell-relevant scale (Baker, Banerjee, Bonin, & Guthold, 2016; Ogneva, Lebedev, & Shenkman, 2010). The tensile modulus of the bulk airbrushed fiber mat was 23.5 MPa. For comparison, the tensile modulus of an electrospun E1001 (1k) mat with randomly oriented fibers was 24.2 MPa. Figure 3c shows the ratios of force to deflection at various points in the sparse fiber mat

prepared for the AFM measurement. The forces were <2 μN and the maximum deflection was 5 μm . These forces are comparable to the adhesion forces of cells on a variety of substrates indicating the fibers will provide sufficient strength for cell motility (Potthoff et al., 2012, 2014). Measurements made close to the struts as well as away from the struts were not statistically different indicating that proximity to the support does not make fibers more rigid. These measurements suggest that the fibers produced by airbrushing are flexible enough to give tactile feedback to the cells that are seeded on the fiber mat.

3.3 | Cell proliferation in hybrid scaffolds

One-week HDF cell cultures on hybrid E1001 (1k) scaffolds were carried out to observe cell organization on infiltration into sterilized scaffolds. Cells were observed across the surface of the hierarchical scaffold, spanning the pores between the FDM struts (Figure 4a,b). After 7 days, full-thickness maximum intensity confocal imaging of scaffold cross-sections showed the presence of cells with a deposited fibronectin matrix at each scaffold layer (Figure 4c). The presence of robust fibronectin matrix indicated that the cells remained viable throughout the thickness of the scaffold.

3.4 | In vivo cellular infiltration into hierarchical scaffolds

The formation of integrated tissues within large defects in vivo necessitates the infiltration of cells and vasculature into scaffolding.

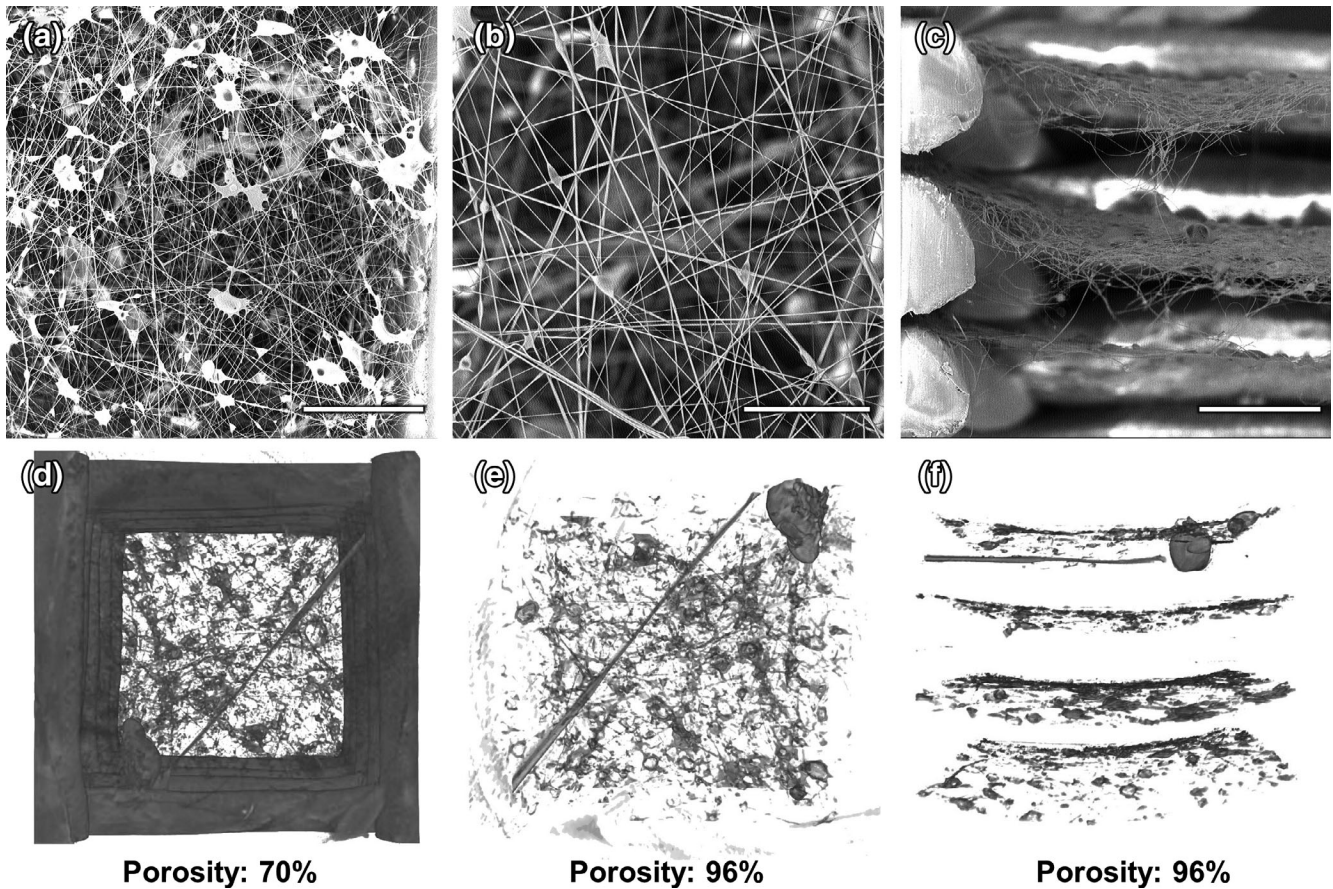


FIGURE 2 Representative images of hierarchical scaffold structure including (a) SEM of airbrushed E1001 (1k) fibers within 3D printed scaffolds (scale bar 300 μm), (b) Magnified view of fibers within the 3D printed structure (scale bar 80 μm), (c) SEM cross-section of fiber mats within 3D printed structure (scale bar 300 μm), (d) Reconstructed micro-CT image of a single hierarchical scaffold unit cell and the corresponding porosity, (e) Reconstructed micro-CT image of fibers only within a single hierarchical scaffold pore and the corresponding porosity, and (f) Reconstructed micro-CT image of fiber mat cross-sections

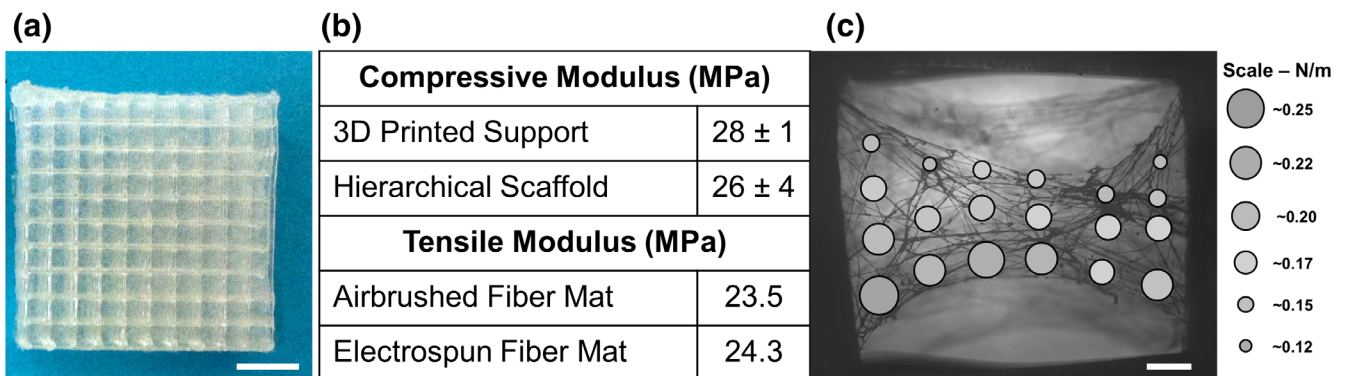


FIGURE 3 Bulk and cell-scale mechanical characterization of hierarchical scaffolds. (a) Top-down view of a completed hierarchical scaffold (Scale bar is 5 mm). (b) Young's modulus of 3D printed PLA struts with or without E1001 (1k) airbrushed fibers ($n = 3 \pm \text{SD}$) and tensile modulus of airbrushed and electrospun E1001 (1k) fiber mats, (c) Atomic Force Microscopy (AFM) modulus map of airbrushed E1001 (1k) fibers (Scale bar is 0.16 mm)

Hierarchical scaffolds and mats of airbrushed fibers alone were implanted subcutaneously in Sprague–Dawley rats for 14 days. Hierarchical scaffolds were infiltrated with vascularized tissue throughout the

cross-sectional area (Figure 5b). In contrast, airbrushed fiber mats alone were encapsulated within a 100 μm fibrous capsule, with very few cells observed to have migrated greater than 300 μm (Figure 5c). The core

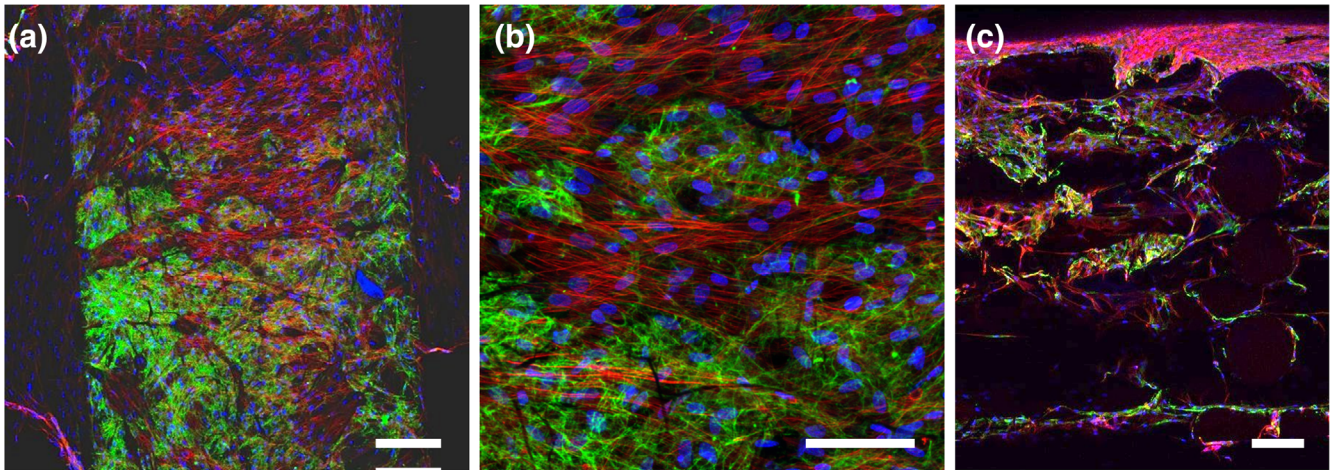


FIGURE 4 Cellular infiltration and ECM deposition within a hierarchical scaffold. Human dermal fibroblasts were grown within the scaffold for 7 days, fixed, and stained for fibronectin (green), actin (red), and nuclei (blue). Confocal images shown are maximum intensity projections (a,b) of the airbrushed fibers between two struts on the scaffold surface. (c) Cross-section of scaffolds showing cell infiltration and fibronectin deposition throughout the depth of the scaffold. Scale bars are 200 μm (a,c) and 100 μm (b)

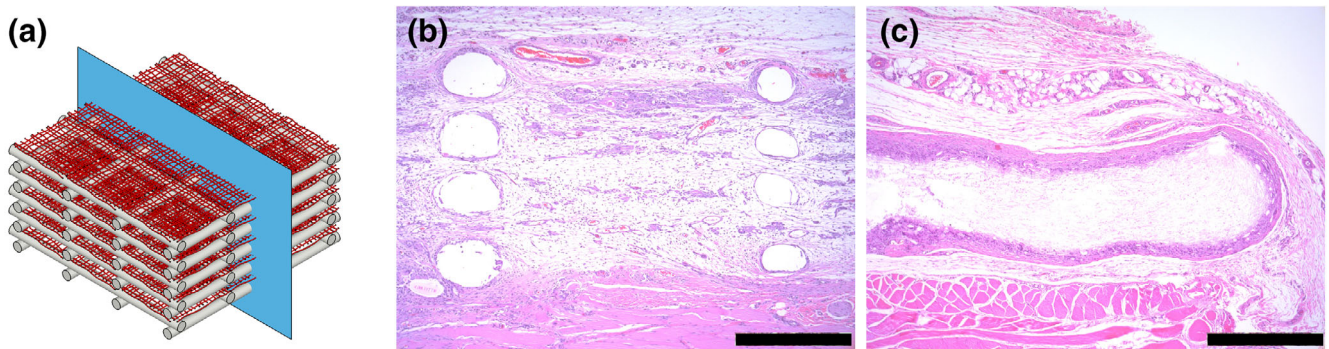


FIGURE 5 In vivo H&E staining indicating differential cellular infiltration into scaffolds. (a) Schematic of scaffold cross-section plane. H&E stained sections of hierarchical (b) and airbrushed only (c) from 14-day rat subcutaneous explants. Scale bar is 500 μm

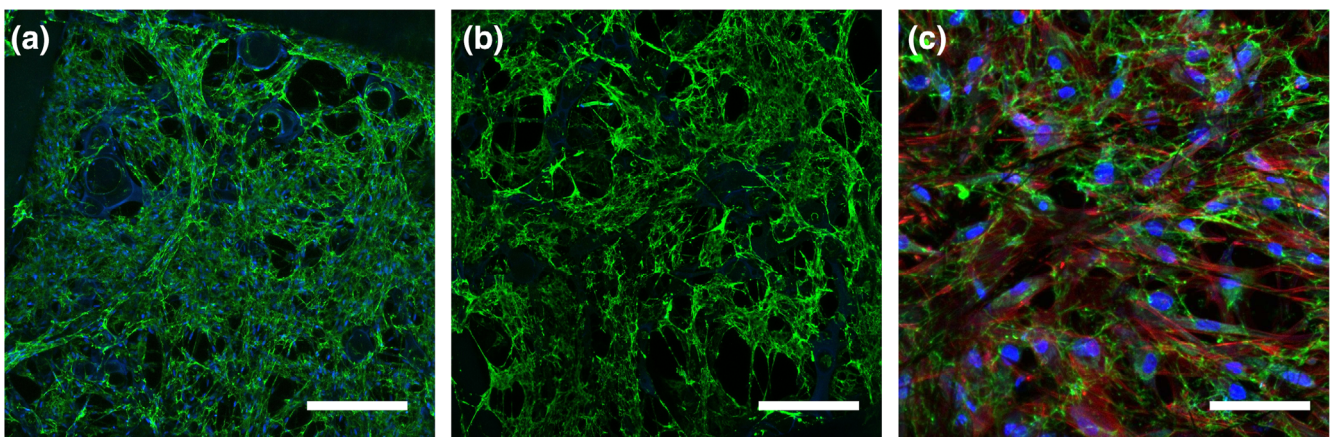


FIGURE 6 HDF infiltration and assembly of a robust ECM before (a) and after (b) decellularization on Day 7. Scaffolds were recellularized with MSC for 24 hr (c). Scaffolds were fixed and stained for fibronectin (green), nuclei (blue) and actin (red, c only). Scale bars are 200 μm (a,c) and 100 μm (b)

of the unsupported airbrushed mat was a dense polymer bundle with no cellular infiltration or vascularization to support tissue development.

3.5 | Scaffold decellularization and recellularization

The functionalizability and the robustness of the hierarchical scaffold were tested by running standardized decellularization and recellularization protocols on scaffold cultured with HDFs (Goyal et al., 2017). After 7 days *in vitro*, scaffolds were decellularized resulting in the removal of the fibroblast cells from the matrix while retaining the base E1001 (1k) fiber mats with ECM on top (Figure 6a, b). Fibronectin fibril density and morphology was maintained throughout the decellularization process. Upon recellularization with mesenchymal stromal cells, the decellularized scaffolds promoted cellular attachment and spreading (Figure 6c). Therefore, the hierarchical scaffolds can withstand standard tissue engineering protocols including decellularization and can be recellularized with application-specific cell types (Mao, Hoffman, Wu, Goyal, & Kohn, 2017).

4 | DISCUSSION

Hierarchical scaffolds were successfully produced by iteratively printing polymer struts while airbrushing polymer fibers between printed layers to create a 1 mm thick fibrous structure with improved cell integration properties. This process provides additional surface area for tissue regeneration within the 3D printed scaffold with >97% porosity between struts and ~70% porosity overall. Airbrushing proved effective at forming microfiber meshes that could be easily incorporated into the 3D printed frames. At only 3 s of airbrushing per layer, the additional fabrication time for the scaffolds was on the order of minutes which aligns well with the rapid fabrication associated with 3D printing. This provides a significant improvement over combined 3D printing and electrospinning setups which can take up to five times longer to fabricate a single fiber mat layer (Medeiros et al., 2009).

Developing airbrushing methods for new polymers requires balancing multiple factors including solution concentration, target distance, and air pressure. When the polymer concentration was low, below 5 wt%, the airbrushed solution failed to form fibers due to insufficient time during flight for adequate solvent evaporation. This resulted in the formation of a thin, continuous polymer film coating the entire device, the end of which was seen in the higher number of defects per fiber. At high polymer concentration, near 10 wt%, the increased solution viscosity combined with rapid solvent evaporation clogged the airbrush tip, leading to sputtering and larger diameter fibers. At the optimal concentration of 6 wt% E1001 (1k), polymer fibers were observed extending from the tip of the airbrush, flying through the air and forming a nonwoven mat on the target substrate. The resulting fiber mat presented the fewest defects and kept the small fiber size essential for promoting cell infiltration. Reduction in fiber defects and control of fiber diameter are important for maintaining the homogeneity of the scaffold, thus ensuring that cell

behavior does not vary due to the underlying substrate and that mechanical properties are consistent throughout. Other groups have investigated how different models of airbrushes and nozzle diameters can affect fiber quality and consistency (Tutak, Gelven, Markle, & Palmer, 2015). While airbrushing was carried out by hand in this study, robotic automation of the process to work in tandem with 3D printing is certainly attainable.

The hierarchical scaffold approach described here ameliorates the problems associated with poor cellular infiltration that has long been a challenge for microfiber and nanofiber implants. In our system, the 3D printed supports take on the role of opening up the microfiber mats while increasing the volume, controlling the shape and protecting the fibers against mechanical wear. Controlling the 3D printed design along with the density of airbrushing during scaffold fabrication as shown in Figure 1 allows for creation of scaffold with pore sizes within the optimum range. Struts produced by FDM provided shape, stability, and spacing to the airbrushed fiber mats while the microfibers filled otherwise empty pore spaces, as shown in Figure 2, providing additional surface area for cell growth. Without the airbrushed fiber mats, the imaged areas of Figures 4 and 6 would be devoid of both cells and ECM.

The airbrushed fiber mats provide a substrate for cell-derived ECM deposition within the 3D printed frames as a preliminary step to integrating the scaffold with the surrounding tissue. Fibroblasts cultured on the hierarchical scaffold showed that the high porosity of the fiber mats allowed for easy cellular penetration throughout the scaffold network. The scaffold cross-section view in Figure 4c clearly shows the presence of not only cells but also a developing ECM on top of the supporting fiber mat sheets. Fibronectin was deposited by HDFs throughout the scaffold within one week of seeding showing the cell compatibility of the E1001 (1k) airbrushed fiber mat. Without the airbrushed fiber mats, the sections between struts would be devoid of any cellular development. Over time, the E1001 (1k) fiber mats will degrade and be resorbed while the ECM will continue to be remodeled, leading to a more natural cell environment. Histological analysis of hierarchical scaffolds placed subcutaneously in the dorsal region of rats in Figure 5b,c showed complete tissue penetration throughout the entire 1 mm thick scaffold. In comparison, airbrushed fiber mats alone showed sparse cellular penetration past 100 μm providing a clear example of the poor cell penetration in traditional fiber mats. Layers of cells and tissue were observed within the explanted hierarchical scaffolds corresponding with the location of the interspersed airbrushed fiber mats. This indicates the hierarchical framework aided cellular infiltration as well as providing an element of spatial control over cell behavior and tissue development within the scaffolds that could potentially be used to engineer complex tissues. The layered architecture can be exploited to engineer anisotropic tissues with gradients of composition, functionality, and morphology.

While the microfiber network and cell-derived ECM within a hierarchical scaffold is intricate, it is also robust. Specifically, upon decellularization, the fibronectin network was maintained along with the underlying airbrushed fiber network. Decellularized fiber mats have been explored as a way to increase the bioactivity of substrates

(Goyal et al., 2017). This presents an intriguing potential to create hybrid scaffolds with both artificial polymer structure and naturally derived ECM functionality. Ideally, the airbrushed fiber mat will be replaced over time by natural ECM as the E1001 (1k) degrades and is resorbed. Providing cell-derived ECM on the scaffold through recell-decell demonstrated method of functionalizing what would otherwise be a blank template with cell cues and attachment points prior to implantation. HDFs were used in our study because of their ability to rapidly-produce a robust matrix, but could be substituted with different cell types for other applications. For example, prior work by our group has shown that cell-derived ECM from chondrocytes and osteoblasts on electrospun fiber mats promote either chondrogenic or osteogenic differentiation of hMSCs (Mao et al., 2017). E1001 (1k) is a promising polymer for scaffold fabrication in bone and cartilage regeneration. It has been used previously by our group for bone regeneration as a salt-leached porous foam scaffold in nonload-bearing applications where it increased ALP, OCN, and mineralized calcium production in vitro and promoted osteoconductive bone growth in vivo (Jinku et al., 2015; Kim et al., 2011; Kim et al., 2015). By harnessing the ability to precondition hierarchical scaffold with osteogenic or chondrogenic cell-derived ECM we could produce scaffold with specific bone or cartilage regenerative properties. Trabecular bone is highly porous, around 80%, with a compressive modulus of 0.22–10.44 MPa which we were able to approximate in our hierarchical scaffold, achieving 70% porosity and 26 MPa compressive modulus (Misch, Qu, & Bidez, 1999; Renders, Mulder, Van Ruijven, & Van Eijden, 2007). In cartilage tissue the natural stiffness is much lower, in the range of 0.1–2 MPa (Zhang, Hu, & Athanasiou, 2009). Chemical functionalization of E1001 (1k) is a potential future route of exploration for increasing the bioactivity of the hierarchical scaffold as well. Unfortunately, E1001 (1k) does not have the melt properties required to be 3D printable which limits its options for scaffold manufacturing. Optimizing an airbrushing protocol for E1001 (1k) and incorporating it into 3D printed frames of PLA or PCL provides a rapid alternative to porogen leaching, electrospinning, or other traditional fabrication methods. The flexibility of our hierarchical scaffold fabrication method makes it possible to mimic the properties of tissues, such as bone and cartilage while providing natural cell cues by altering polymer used, scaffold geometry, fiber density, and cell seeding type.

5 | CONCLUSION

Hierarchical scaffolds were fabricated for tissue engineering applications by combining the ability of fiber mats to support cells with the mechanical strength, open pore structure, and customizability of the 3D printed frame. Airbrushing process variables including polymer concentration, air pressure, spray distance, and duration were optimized for E1001 (1k) to obtain reduced defect microfiber mats. These fiber mats were easily and rapidly interspersed within the 3D scaffold during the printing process. Combining the two fabrication methods allows these scaffolds to be highly customizable by employing a wide variety of materials in nearly limitless geometries. Cells easily

penetrate the distributed microfibers in vitro as a result of spacing provided by the 3D printed scaffold. In vivo testing showed improved cell penetration and tissue integration into hierarchical scaffold relative to controls. In vitro cultured HDFs deposited extensive fibronectin matrix throughout the airbrushed fibers. Scaffolds, airbrushed fibers, and the cell-derived ECM were robust enough to survive decellularization and recellularization, increasing the functionality and versatility of this tissue-engineering platform. By combining FDM and airbrushing techniques, we have rapidly engineered customizable scaffolds that support increased cell growth and infiltration.

ACKNOWLEDGMENTS

We thank Nanosurf (Dr. Saju Nettikadan) for loaning us the AFM, and Dr. Edward Nelson for helping us with the measurements. This study was supported by RESBIO, the "Resource for polymeric biomaterials" funded by the National Institute of Health, National Institute of Biomedical Imaging and Bioengineering Award Number P41EB001046. The authors would like to thank Daniel Martin for assistance with confocal imaging.

REFERENCES

- Acun, A., & Hasirci, V. (2014). Construction of a collagen-based, split-thickness cornea substitute. *Journal of Biomaterials Science, Polymer Edition*, 25(11), 1110–1132.
- Agarwal, S., Wendorff, J. H., & Greiner, A. (2008). Use of electrospinning technique for biomedical applications. *Polymer*, 49(26), 5603–5621.
- Agarwal, S., Wendorff Joachim, H., & Greiner, A. (2009). Progress in the Field of Electrospinning for Tissue Engineering Applications. *Advanced Materials*, 21(32-33), 3343–3351.
- Ahn, C. B., Son, K. H., Yu, Y. S., Kim, T. H., Lee, J. I., & Lee, J. W. (2019). Development of a flexible 3D printed scaffold with a cell-adhesive surface for artificial trachea. *Biomedical Materials*, 14(5), 055001.
- Baker, S. R., Banerjee, S., Bonin, K., & Guthold, M. (2016). Determining the mechanical properties of electrospun poly-ε-caprolactone (PCL) nanofibers using AFM and a novel fiber anchoring technique. *Materials Science and Engineering: C*, 59, 203–212.
- Beachley, V., & Wen, X. (2009). Effect of electrospinning parameters on the nanofiber diameter and length. *Materials Science & Engineering. C, Materials for Biological Applications*, 29(3), 663–668.
- Behrens, A. M., Casey, B. J., Sikorski, M. J., Wu, K. L., Tutak, W., Sandler, A. D., & Kofinas, P. (2014). In situ deposition of PLGA nanofibers via solution blow spinning. *ACS Macro Letters*, 3(3), 249–254.
- Behrens, A. M., Kim, J., Hotaling, N., Seppala, J. E., Kofinas, P., & Tutak, W. (2016). Rapid fabrication of poly(DL-lactide) nanofiber scaffolds with tunable degradation for tissue engineering applications by air-brushing. *Biomedical materials (Bristol, England)*, 11(3), 035001–035001.
- Chen, C., Townsend, A. D., Sell, S. A., & Martin, R. S. (2017). Microchip-based 3D-cell culture using polymer nanofibers generated by solution blow spinning. *Analytical Methods*, 9(22), 3274–3283.
- Chen, W., Xu, Y., Liu, Y., Wang, Z., Li, Y., Jiang, G., ... Zhou, G. (2019). Three-dimensional printed electrospun fiber-based scaffold for cartilage regeneration. *Materials & Design*, 179, 107886.
- Chia, H. N. (2015). Wu BM. Recent advances in 3D printing of biomaterials. *Journal of Biological Engineering*, 9, 4.

- Daristotle, J. L., Behrens, A. M., Sandler, A. D., & Kofinas, P. (2016). A review of the fundamental principles and applications of solution blow spinning. *ACS Applied Materials & Interfaces*, 8(51), 34951–34963.
- De Mori, A., Peña Fernández, M., Blunn, G., Tozzi, G., & Roldo, M. (2018). 3D printing and electrospinning of composite hydrogels for cartilage and bone tissue engineering. *Polymers*, 10(3), 285.
- de Valence, S., Tille, J.-C., Mugnai, D., Mrowczynski, W., Gurny, R., Möller, M., & Walpoth, B. H. (2012). Long term performance of polycaprolactone vascular grafts in a rat abdominal aorta replacement model. *Biomaterials*, 33(1), 38–47.
- Goyal, R., Vega, M. E., Pastino, A. K., Singh, S., Guvendiren, M., Kohn, J., ... Schwarzbauer, J. E. (2017). Development of hybrid scaffolds with natural extracellular matrix deposited within synthetic polymeric fibers. *Journal of Biomedical Materials Research Part A*, 105(8), 2162–2170.
- Hutmacher Dietmar, W., Schantz, T., Zein, I., Ng Kee, W., Teoh Swee, H., & Tan Kim, C. (2001). Mechanical properties and cell cultural response of polycaprolactone scaffolds designed and fabricated via fused deposition modeling. *Journal of Biomedical Materials Research*, 55(2), 203–216.
- Jeong, Y.-I., Kang, M.-K., Sun, H.-S., Kang, S.-S., Kim, H.-W., Moon, K.-S., ... Jung, S. (2004). All-trans-retinoic acid release from core-shell type nanoparticles of poly(ϵ -caprolactone)/poly(ethylene glycol) diblock copolymer. *International Journal of Pharmaceutics*, 273(1), 95–107.
- Jinku, K., Sean, M., Amy, D., Aniq, D., Maria Hanshella, R. M., & Jeffrey, O. H. (2015). Tyrosine-derived polycarbonate scaffolds for bone regeneration in a rabbit radius critical-size defect model. *Biomedical Materials*, 10(3), 035001.
- Karageorgiou, V., & Kaplan, D. (2005). Porosity of 3D biomaterial scaffolds and osteogenesis. *Biomaterials*, 26(27), 5474–5491.
- Kim, J., Magno, M. H. R., Alvarez, P., Darr, A., Kohn, J., & Hollinger, J. O. (2011). Osteogenic differentiation of pre-osteoblasts on biomimetic tyrosine-derived polycarbonate scaffolds. *Biomacromolecules*, 12(10), 3520–3527.
- Kim, J., Magno, M. H. R., Ortiz, O., McBride, S., Darr, A., Kohn, J., & Hollinger, J. O. (2015). Next-generation resorbable polymer scaffolds with surface-precipitated calcium phosphate coatings. *Regenerative Biomaterials*, 2(1), 1–8.
- Kong, B., Sun, W., Chen, G., Tang, S., Li, M., Shao, Z., & Mi, S. (2017). Tissue-engineered cornea constructed with compressed collagen and laser-perforated electrospun mat. *Scientific Reports*, 7(1), 970.
- Kuznetsov, V., Solonin, A., Urzhumtsev, O., Schilling, R., & Tavitov, A. (2018). Strength of PLA components fabricated with fused deposition technology using a desktop 3D printer as a function of geometrical parameters of the process. *Polymers*, 10(3), 313.
- Lannutti, J., Reneker, D., Ma, T., Tomasko, D., & Farson, D. (2007). Electrospinning for tissue engineering scaffolds. *Materials Science and Engineering: C*, 27(3), 504–509.
- Magno, M. H. R., Kim, J., Srinivasan, A., McBride, S., Bolikal, D., Darr, A., ... Kohn, J. (2010). Synthesis, degradation and biocompatibility of tyrosine-derived polycarbonate scaffolds. *Journal of Materials Chemistry*, 20(40), 8885–8893.
- Mao, Y., Hoffman, T., Wu, A., Goyal, R., & Kohn, J. (2017). Cell type-specific extracellular matrix guided the differentiation of human mesenchymal stem cells in 3D polymeric scaffolds. *Journal of Materials Science. Materials in Medicine*, 28(7), 100–100.
- Mao, Y., & Schwarzbauer, J. E. (2005). Stimulatory effects of a three-dimensional microenvironment on cell-mediated fibronectin fibrillogenesis. *Journal of Cell Science*, 118(19), 4427.
- Medeiros, E. S., Glenn, G. M., Klamczynski, A. P., Orts, W. J., & Mattoso, L. H. C. (2009). Solution blow spinning: A new method to produce micro- and nanofibers from polymer solutions. *Journal of Applied Polymer Science*, 113(4), 2322–2330.
- Mellor, L., Huebner, P., Cai, S., Mohiti-Asli, M., Taylor, M., Spang, J., ... Lobo, E. (2017). Fabrication and evaluation of electrospun, 3D-bioplotted, and combination of electrospun/3D-bioplotted scaffolds for tissue engineering applications. *BioMed Research International*, 2017, 1–9.
- Misch, C. E., Qu, Z., & Bidez, M. W. (1999). Mechanical properties of trabecular bone in the human mandible: Implications for dental implant treatment planning and surgical placement. *Journal of Oral and Maxillofacial Surgery*, 57(6), 700–706.
- Moroni, L., Schotel, R., Hamann, D., de Wijn, J. R., & van Blitterswijk, C. A. (2008). 3D fiber-deposited electrospun integrated scaffolds enhance cartilage tissue formation. *Advanced Functional Materials*, 18(1), 53–60.
- Ogneva, I. V., Lebedev, D. V., & Shenkman, B. S. (2010). Transversal stiffness and Young's modulus of single fibers from rat soleus muscle probed by atomic force microscopy. *Biophysical Journal*, 98(3), 418–424.
- Oh, S. H., Park, I. K., Kim, J. M., & Lee, J. H. (2007). In vitro and in vivo characteristics of PCL scaffolds with pore size gradient fabricated by a centrifugation method. *Biomaterials*, 28(9), 1664–1671.
- Oliveira, J. E., Moraes, E. A., Costa, R. G. F., Afonso, A. S., Mattoso, L. H. C., Orts, W. J., & Medeiros, E. S. (2011). Nano and submicrometric fibers of poly(D,L-lactide) obtained by solution blow spinning: Process and solution variables. *Journal of Applied Polymer Science*, 122(5), 3396–3405.
- Park, S. Y., Ki, C. S., Park, Y. H., Jung, H. M., Woo, K. M., & Kim, H. J. (2009). Electrospun silk fibroin scaffolds with macropores for bone regeneration: An in vitro and in vivo study. *Tissue Engineering Part A*, 16(4), 1271–1279.
- Potthoff, E., Franco, D., D'Alessandro, V., Starck, C., Falk, V., Zambelli, T., ... Ferrari, A. (2014). Toward a rational design of surface textures promoting endothelialization. *Nano Letters*, 14(2), 1069–1079.
- Potthoff, E., Guillaume-Gentil, O., Ossola, D., Polesel-Maris, J., LeibundGut-Landmann, S., Zambelli, T., & Vorholt, J. A. (2012). Rapid and serial quantification of adhesion forces of yeast and mammalian cells. *PLoS One*, 7(12), e52712.
- Rampichová, M., Košťáková Kuželová, E., Filová, E., Chvojka, J., Šafka, J., Pelcl, M., ... Amler, E. (2018). Composite 3D printed scaffold with structured electrospun nanofibers promotes chondrocyte adhesion and infiltration. *Cell Adhesion & Migration*, 12(3), 271–285.
- Renders, G. A. P., Mulder, L., Van Ruijven, L. J., & Van Eijden, T. M. G. J. (2007). Porosity of human mandibular condylar bone. *Journal of Anatomy*, 210(3), 239–248.
- Rnjak-Kovacina, J., & Weiss, A. S. (2011). Increasing the pore size of electrospun scaffolds. *Tissue Engineering Part B: Reviews*, 17(5), 365–372.
- Sheihet, L., Chandra, P., Batheja, P., Devore, D., Kohn, J., & Michniak, B. (2008). Tyrosine-derived nanospheres for enhanced topical skin penetration. *International journal of pharmaceutics*, 350(1), 312–319.
- Sill, T. J., & von Recum, H. A. (2008). Electrospinning: Applications in drug delivery and tissue engineering. *Biomaterials*, 29(13), 1989–2006.
- Soletti, L., Nieponice, A., Hong, Y., Ye, S.-H., Stankus, J. J., Wagner, W. R., & Vorp, D. A. (2011). In vivo performance of a phospholipid-coated bioerodable elastomeric graft for small-diameter vascular applications. *Journal of biomedical materials research. Part A*, 96(2), 436–448.
- Tutak, W., Gelven, G., Markle, C., & Palmer, X. L. (2015). Rapid polymer fiber airbrushing: Impact of a device design on the fiber fabrication and matrix quality. *Journal of Applied Polymer Science*, 132(47), 42813.
- Wang, X., Ding, B., & Li, B. (2013). Biomimetic electrospun nanofibrous structures for tissue engineering. *Materials Today*, 16(6), 229–241.
- Wray, L. S., & Orwin, E. J. (2009). Recreating the Microenvironment of the Native Cornea for Tissue Engineering Applications. *Tissue Engineering Part A*, 15(7), 1463–1472.
- Yang, F., Murugan, R., Wang, S., & Ramakrishna, S. (2005). Electrospinning of nano/micro scale poly(L-lactic acid) aligned fibers and their potential in neural tissue engineering. *Biomaterials*, 26(15), 2603–2610.
- Yoshimoto, H., Shin, Y. M., Terai, H., & Vacanti, J. P. (2003). A biodegradable nanofiber scaffold by electrospinning and its potential for bone tissue engineering. *Biomaterials*, 24(12), 2077–2082.

- Yu, C., & Kohn, J. (1999). Tyrosine-PEG-derived poly (ether carbonate) s as new biomaterials: Part I: synthesis and evaluation. *Biomaterials*, 20 (3), 253-264.
- Zhang, L., Hu, J., & Athanasiou, K. A. (2009). The role of tissue engineering in articular cartilage repair and regeneration. *Critical reviews in biomedical engineering*, 37(1-2), 1-57.
- Zhang, W., Zhang, Z., Chen, S., Macri, L., Kohn, J., & Yelick, P. C. (2016). Mandibular jaw bone regeneration using human dental cell-seeded tyrosine-derived polycarbonate scaffolds. *Tissue Engineering. Part A*, 22 (13-14), 985-993.
- Zhu, X., Cui, W., Li, X., & Jin, Y. (2008). Electrospun fibrous mats with high porosity as potential scaffolds for skin tissue engineering. *Bio-macromolecules*, 9(7), 1795-1801.

SUPPORTING INFORMATION

Additional supporting information may be found online in the Supporting Information section at the end of this article.

How to cite this article: Molde J, Steele JAM, Pastino AK, Mahat A, Murthy NS, Kohn J. A step toward engineering thick tissues: Distributing microfibers within 3D printed frames. *J Biomed Mater Res*. 2020;108A:581-591. <https://doi.org/10.1002/jbm.a.36838>